Band structure of LaB_6 by an algorithm for filtering reconstructed electron-positron momentum densities

G. Kontrym-Sznajd and M. Samsel-Czekała
W. Trzebiatowski Institute of Low Temperature and Structure Research, Polish Academy of Sciences, P.O. Box 1410, 50-950 Wrocław 2, Poland

M. Biasini
ENEA, via don Fiammelli 2, IT-40128 Bologna, Italy

Y. Kubo
Department of Physics, Colleges of Humanities and Sciences, Nihon University, Tokyo 156, Japan
(Received 13 January 2004; published 8 September 2004)

A new method for filtering three-dimensional reconstructed densities is proposed. The algorithm is tested with simulated spectra and employed to study the electronic structure of the rare-earth compound LaB_6. For this system, momentum densities are reconstructed from theoretical and experimental two-dimensional angular correlation of electron-positron annihilation radiation (2D ACAR) spectra. The experimental results are in good agreement with the band structure calculated with the full-potential linearized augmented-plane-wave (FLAPW) method within the local-density approximation (LDA), apart from the detection of small electron pockets in the 15th band. It is also shown that, unlike the electron-positron enhancement, the electron-electron correlations affect noticeably the momentum density.

DOI: 10.1103/PhysRevB.70.125103 PACS number(s): 78.70.Bj, 74.25.Jb, 87.59.Fm

I. INTRODUCTION

LaB_6 belongs to rare-earth hexaborides, of the type RB_6 having a simple cubic crystal structure ($Pm3m$). The B_6 octahedra and rare-earth atoms form interpenetrating simple cubic sublattices. The hexaborides have attracted a lot of attention, owing a variety of behaviours, ranging from paramagnetism (LaB_6), magnetic ordering (PrB_6, NdB_6) and heavy fermion behavior (CeB_6). The electronic structure of the non-f-electron system LaB_6 was probed by several de Haas van Alphen (dHvA) and acoustic dHvA (Refs. 1–11) as well as 2D ACAR (Refs. 12–14) experiments. First, six 2D ACAR spectra were measured and interpreted in terms of reconstructed densities $\rho(\mathbf{k})$.[12] Then, two 2D ACAR spectra, measured for the [100] and [110] integration directions, were analyzed in the form of line projections of $\rho(\mathbf{k})$.[13] Recently, the three-dimensional (3D) image of the Fermi surface (FS) was displayed utilizing three 2D ACAR projections and two different reconstruction methods.[14]

Experimental results were compared with band-structure calculations.[8,15,16] According to the standard FLAPW (within LDA) method,[16] the FS, generated by a single (14th) conduction band, consists of a set of symmetrical electron ellipsoids centered at X points of the cubic Brillouin zone (BZ) and connected by short necks. There is a strong hybridization of the B p and La df states, where f states are unoccupied. In addition to the main FS sheet, a joint application of theory and dHvA experiments[8,10] established the existence of a second sheet of 12 smaller electron pockets along the ΓM directions. These FS elements, obtained by displacing the energy parameter of the $4f$ orbitals upward by 0.1 Ry and including the spin-orbit interaction in the self-consistent band structure calculations, were not detected in the previous 2D ACAR experiments.[12,13]

In this paper we analyze e-p momentum densities in LaB_6, reconstructed from both two theoretical (consistent with band structure results presented in Ref. 16) and the three experimental 2D ACAR spectra from Ref. 14 and interpret them both in the extended **p** and reduced **k** spaces. A new method of filtering densities reconstructed from their line projections is proposed and applied to cubic model and 2D ACAR data in LaB_6.

II. RECONSTRUCTION TECHNIQUE

In the last decades, the mathematical problem of reconstruction of densities from their line projections has extensively been investigated for its relevance to medical diagnostic studies.[17–19] Similar methods are utilized to study the electronic structure of solids where, by using the positron annihilation technique,[20] one measures line integrals of a density as well:

$$N(p_y',p_z') = \int_{-\infty}^{\infty} dp_x' \rho(\mathbf{p}). \tag{1}$$

Here $\rho(\mathbf{p})$ is the electron momentum density in the extended zone scheme (defined in the crystal system **p**), as *seen* by positron, and $N(p_y',p_z')$ describes two-dimensional angular correlation of annihilation radiation (2D ACAR) spectrum measured in the laboratory frame $\mathbf{p}'$.

In most cases, the 3D density is yielded by reconstructing separately its 2D subsections from 1D line integrals. For example, in Cormack's method (CM) (Ref. 21) both functions N and ρ are expanded into the polar Fourier series. Choosing planes $p_z'=$const., perpendicular to the main rotation axis of the crystal p_z (on such planes number of equivalent direc-

tions is maximum), both series reduce to cosine series[22]

$$\rho(p_x,p_y,p_z=\text{const.}) \equiv \rho(\tilde{p},\varphi) = \sum_{n=0}^{\infty} \rho_n(\tilde{p})\cos(n\varphi) \qquad (2)$$

and

$$N(p_y',p_z'=\text{const.}) \equiv N(t,\beta) = \sum_{n=0}^{\infty} N_n(t)\cos(n\beta), \qquad (3)$$

with $n=iR$, where R denotes the order of the main rotation axis [001] ($i=0,1,2,\ldots$, etc.). Here both functions are described in the polar system (p_x, p_y), defined on each of the planes $p_z'=p_z=[001]$. The variables $t=|p_y'|$ and β denote the distance of the integration line from the origin of this polar coordinate system and its angle with respect to the fixed axis p_x, respectively, and $\tilde{p}=\sqrt{p_x^2+p_y^2}$.

If $N_n(t)$ is expanded into a series of Chebyshev polynomials of the second kind ($U_l(t)$):

$$N_n(t) = 2\sum_{m}^{\infty} a_n^m \sqrt{1-t^2}\,U_{n+2m}(t), \qquad (4)$$

then Eq. (1) can be solved analytically and

$$\rho_n(\tilde{p}) = \sum_{m}^{\infty} (n+2m+1)a_n^m R_n^m(\tilde{p}), \qquad (5)$$

where $R_n^m(\tilde{p})$ are Zernike polynomials.

Having 2D densities on each of the planes $p_z=\text{const.}=p_z^c$, one is able to construct the 3D quantity,

$$\rho(\tilde{p},p_z^c) = \sum_{n=0} \rho_n(\tilde{p},p_z^c)\cos(n\varphi), \qquad (6)$$

which can be described in the spherical system

$$\rho(p,\Theta,\varphi) = \sum_{n=0} \rho_n(p,\Theta)\cos(n\varphi), \qquad (7)$$

where $p=\sqrt{\tilde{p}^2+p_z^2}$ and $(\Theta=\arctan(\tilde{p}/p_z),\varphi)$ are the azimuthal and polar angles of $\mathbf{p}$ with respect to the reciprocal lattice coordinate system.

Having functions $\rho_n(p,\Theta)$, reconstructed via Cormack's or other reconstruction algorithms,[23] one can improve reconstructed densities by the new filtering method that will be described in the next chapter and then applied to both cubic model and 2D ACAR spectra for LaB_6.

III. NEW METHOD OF FILTERING RECONSTRUCTED DENSITIES

In crystalline solids various physical quantities are invariant under a suitably chosen projection operator, which is a sum (with appropriate coefficients) of transformations of the point group of the crystal. The electron density ρ (and its plane integrals) have the full symmetry of the BZ (the symmetry of the Γ_1 type where the screw-rotation axes and glide-reflection planes are replaced by plain rotation axes and reflection planes) which can be described by a series of lattice harmonics of a given symmetry:

$$\rho(\mathbf{p}) \equiv \rho(p,\Theta,\varphi) = \sum_{l,\nu} \rho_{l,\nu}(p)F_{l,\nu}(\Theta,\varphi). \qquad (8)$$

The index ν distinguishes harmonics of the same order, $\rho_{l,\nu}(p)$ are the radial coefficients of 3D densities and

$$\rho_{l,\nu}(p) = \int_0^{2\pi}\int_0^{\pi} \rho(p,\Theta,\varphi)F_{l,\nu}(\Theta,\varphi)\sin(\Theta)d\Theta d\varphi. \qquad (9)$$

In the case of structures with one R-fold axis (tetragonal, trigonal or hcp lattices) the lattice harmonics have the form:

$$F_{l,\nu} = \begin{cases} \sqrt{\dfrac{(2l+1)}{4\pi}}P_l(\cos\Theta) \\ \sqrt{\dfrac{(2l+1)(l-|m|)!}{2\pi(l+|m|)!}}P_l^{|m|}(\cos\Theta)\cos(m\varphi), \end{cases} \qquad (10)$$

where, respectively, $l=2i$ and $l=R+2i$ with $m=R+Ri$ and $m\leqslant l$ ($i=0,1,2,\ldots$). $P_l^{|m|}$ are associated Legendre polynomials and R is equal to 6, 4, and 3 for hcp, tetragonal, and trigonal systems, respectively. Here, the subscript $\nu=1,2,3,\ldots$ labels harmonics with the same l.

Such a form of the lattice harmonics allows to express functions $\rho_n(p,\Theta)$ [defined in Eq. (7)] as

$$\rho_n(p,\Theta) = \sum_{l=n}^{\infty} c_l^n \rho_{l,\nu}(p)P_l^n(\cos\Theta), \qquad (11)$$

where c are normalization factors defined in the Eq. (10). Denoting $c_l^nP_l^n(\cos\Theta)\equiv g_l^n$, e.g., for the tetragonal structure ($R=4$) three first density components are the following:

$$\rho_0(p,\Theta) = \rho_{0,1}(p) + g_2^0\rho_{2,1}(p) + g_4^0\rho_{4,1}(p) + \cdots,$$

$$\rho_4(p,\Theta) = g_4^4\rho_{4,2}(p) + g_6^4\rho_{6,2}(p) + g_8^4\rho_{8,2}(p) + \cdots,$$

$$\rho_8(p,\Theta) = g_8^8\rho_{8,3}(p) + g_{10}^8\rho_{10,3}(p) + g_{12}^8\rho_{12,3}(p) + \cdots.$$

For the cubic structures, having three fourfold axes, the lattice harmonics are linear combinations of the associated Legendre polynomials.[24] Moreover, since for some index l there are a few independent lattice harmonics with the same polynomials $P_l^m(x)$, in expressions for $\rho_n(p,\Theta)$ there are also terms with linear combinations of the radial functions $\rho_{l,\nu}(p)$ of the same order l,

$$\rho_n(p,\Theta) = \sum_{l=n}^{\infty}\sum_{\nu} d_{l,\nu}^n c_l^n \rho_{l,\nu}(p)P_l^n(\cos\Theta). \qquad (12)$$

d are the coefficients of symmetrized spherical harmonics, referred to as cubic harmonics and given in Table I in Ref. 24.

TABLE I. Occurrence of radial components $\rho_{l,\nu}(p)$ in $\rho_n(p,\Theta)$ (marked by symbol "+") for cubic structures (according to Table I in Ref. 24).

$\rho_{l,\nu}(p)$ for (l,ν)	$\rho_0(p,\Theta)$	$\rho_4(p,\Theta)$	$\rho_8(p,\Theta)$	$\rho_{12}(p,\Theta)$	$\rho_{16}(p,\Theta)$
(0,1)	+				
(4,1)	+	+			
(6,1)	+	+			
(8,1)	+	+	+		
(10,1)	+	+	+		
(12,1)	+	+	+	+	
(12,2)		+	+	+	
(14,1)	+	+	+	+	
(16,1)	+	+	+	+	+
(16,2)		+	+	+	+

In this case three first density components are equal to

$$\rho_0(p,\Theta) = \rho_{0,1}(p) + d^0_{4,1}g^0_4\rho_{4,1}(p) + d^0_{6,1}g^0_6\rho_{6,1}(p) + \cdots,$$

$$\rho_4(p,\Theta) = d^4_{4,1}g^4_4\rho_{4,1}(p) + d^4_{6,1}g^4_6\rho_{6,1}(p) + d^4_{8,1}g^4_8\rho_{8,1}(p) + d^4_{10,1}g^4_{10}\rho_{10,1}(p) + (d^4_{12,1}\rho_{12,1}(p) + d^4_{12,2}\rho_{12,2}(p))g^4_{12} + \cdots,$$

$$\rho_8(p,\Theta) = d^8_{8,1}g^8_8\rho_{8,1}(p) + d^8_{10,1}g^8_{10}\rho_{10,1}(p) + \cdots.$$

For cubic symmetries, contrary to the case of other structures, functions $\rho_n(p,\Theta)$ strongly depend on each other, which is illustrated in Table I. For example, all radial functions $\rho_{l,1}(p)$ that occur in $f_{n\neq 0}(p,\Theta)$, occur also in $f_0(p,\Theta)$.

Using the orthogonality relation for the associated Legendre polynomials[25]

$$\int_0^1 P^m_l(x)P^k_n(x)dx = \delta_{ln}\delta_{mk}\frac{1}{2l+1}\frac{(l+|m|)!}{(l-|m|)!}, \qquad (13)$$

where $x=\cos\Theta$ and the factor $(4\pi)^{-1/2}$ is omitted, one can estimate the radial components $\rho_{l,\nu}(p)$. The above equation defines the normalization constants c_l and $c^n_l/2$ [see Eqs. (10) and (11)].

For structures with one R-fold axis:

$$\rho_{l,1}(p) = \int_0^{\pi/2} c_l P_l(\cos\Theta)\rho_0(p,\Theta)\sin\Theta d\Theta \qquad (14)$$

and for $\nu>1$,

$$\rho_{l,\nu}(p) = \frac{1}{2}\int_0^{\pi/2} c^n_l P^n_l(\cos\Theta)\rho_n(p,\Theta)\sin\Theta d\Theta. \qquad (15)$$

In the case of cubic structures the corresponding formulas are the same but ρ_l and $\rho_{l,\nu}$ are replaced by $d_{l,1}\rho_{l,1}(p)$ and $\Sigma_\nu d^n_{l,\nu}\rho_{l,\nu}(p)$, respectively.

The most efficient way of calculating polynomials $P_l(x)$ is to use their recurrence relation[25]

$$P_l(x) = \frac{2l-1}{l}xP_{l-1}(x) - \frac{l-1}{l}P_{l-2}(x),$$

where $P_0=1$ and $P_1=x$.

In order to obtain functions $c^m_m P^m_m(x)$, denoted below as W^m_m:

$$W^m_m(x) = (4m+2)^{1/2}\frac{\sin^m(\Theta)}{2^m}\frac{[(2m)!]^{1/2}}{m!},$$

the following iteration procedure is used:

$$W^m_m(i) = W^m_m(i-1)\frac{\sin(\Theta)}{2}\left(\frac{i+m}{i}\right)^{1/2}$$

with changing i up to m, where in the zero step $W^m_m(i=0) = (4m+2)^{1/2}$.

Next polynomials are evaluated from the relation

$$W^m_{m+1}(x) = (2m+3)^{1/2}xW^m_m(x)$$

and for $n=m+2$ up to $n\leqslant l$:

$$W^m_n(x) = \left(\frac{4n^2-1}{n^2-m^2}\right)^{1/2}xW^m_{n-1}(x) - \left[\frac{(n-1)^2-m^2}{n^2-m^2}\right]^{1/2}\left(\frac{2n+1}{2n-3}\right)^{1/2}W^m_{n-2}(x).$$

Summarizing, the steps to apply the new method are described as follows:

(1) Reconstruct density components $\rho_n(\tilde{p})$ {with Cormack's [Eq. (5)] or other methods} on each plane $p_z = \text{const.} = p^c_z$ independently, getting $\rho_n(\tilde{p},p^c_z)$. Express them in the spherical coordinate system, obtaining $\rho_n(p,\Theta)$, defined in Eq. (7).

(2) Invert Eq. (11) or (12) to get [via Eqs. (14) and (15)] the $\rho_{l,\nu}(p)$ coefficients.

(3) Construct new functions $\rho_n(p,\Theta)$ using Eq. (11) or (12) from the calculated $\rho_{l,\nu}(p)$ and, finally, create new 3D densities $\rho(\mathbf{p}\equiv(p,\Theta,\varphi))$ [Eq. (7)].

In the case of structures with one R-fold rotation axis, for each independent function $\rho_n(p,\Theta)$ its radial components $\rho_{l,\nu}(p)$ are calculated separately. Then a new $\rho_n(p,\Theta)$ can be created from $\rho_{l,\nu}(p)$ neglecting components with l above which $\rho_{l,\nu}(p)$ are smaller than the experimental noise. For the cubic structures, where $\rho_n(p,\Theta)$ are strongly dependent on each other, the possibility of improving densities is much greater. In this case, one can determine radial components $\rho_{l,\nu}(p)$ of the same order l simultaneously from all functions $\rho_n(p,\Theta)$ in which they occur (see Table I). For example, $\rho_{12,1}(p)$ together with $\rho_{12,2}(p)$ can be evaluated from four functions $\rho_n(p,\Theta)$ with $n=0$, 4, 8, 12. Therefore, each component $\rho_{l,\nu}(p)$ is determined not only from the values of a given function $\rho_n(p,\Theta)$ for all angles Θ but also from several $\rho_n(p,\Theta)$. Having thus obtained radial components one is able not only to filter primary functions $\rho_n(p,\Theta)$ but additionally create new $\rho_n(p,\Theta)$ of a higher order n.

In the following, CM and NM denote standard Cormack's method and the new filtering method applied to densities reconstructed by the Cormack's technique, respectively.

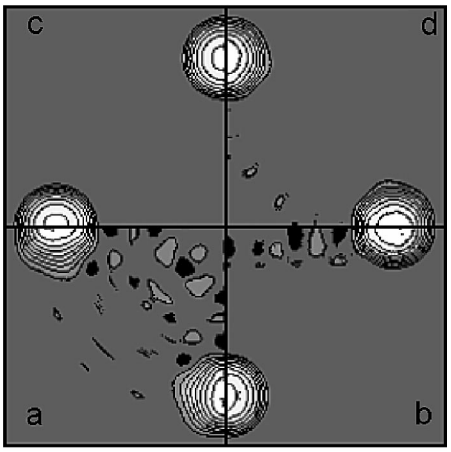

FIG. 1. Densities reconstructed, via the CM, from five projections for model density displayed in part (c). Parts (a) and (b) present, respectively, reconstructed densities on the first plane (001) and on the perpendicular plane (100), i.e., densities along [100] reconstructed independently on succeeding planes, parallel to (001). Part (d) shows results after applying symmetry requirement described by Eq. (16).

IV. APPLICATION TO MODEL

Usually, when the reconstruction method described in Chapter II (or equivalent Ref. 23) is applied to cubic systems, one imposes on the reconstructed density the following symmetry requirement (e.g., Ref. 26):

$$\rho(p_x,p_y,p_z) = \rho(p_y,p_z,p_x) = \rho(p_x,p_z,p_y). \qquad (16)$$

This condition follows from the symmetry of the cubic structures, i.e., nonequivalent fraction of the BZ is equal to $1/48$ [Eq. (16)], instead of $1/16$ [Eq. (2)]. However, such a treatment is not equivalent to that proposed in this paper as shown further. The results of imposing the requirement (16) on model densities reconstructed via the CM are presented in Fig. 1.

It appears that the main discrepancy with the model [part (c)] is observed on the first reconstruction plane [part (a)]. This is due to the difficulty to describe the high anisotropy of our model by only five components $\rho_n(\tilde{p})$ in Eq. (2). A similar situation takes place on a few next reconstruction planes—see results around the horizontal axis in the part (b). However, on the higher reconstruction plane $p_z = p^*$ (and neighboring planes) the model density [sphere centered at $p=(0,0,p^*)$] is isotropic and can be described only by one component. Thus, here one is able to reproduce the same element (as on the first reconstruction plane) with very high precision. Due to this reason results after the symmetry requirement [part (d)] are always improved. In the case of experimental data such a procedure additionally reduces the statistical noise.

This treatment is equivalent to the following: densities, after requirement (16), take into account the cubic symmetry. However, since they are not described by the lattice harmonics series there is no dependence between densities in points (p,Θ,φ) lying in the same irreducible part of the BZ and having the same p (it is not so in the case of the NM).

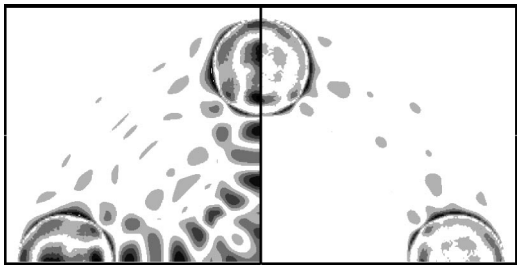

FIG. 2. Absolute differences between model and reconstructed densities on the (001) plane. Left and right sides show results for the CM and NM, respectively. In both cases the symmetry requirement (16) was imposed on reconstructed densities. The darker colors denote the higher values, which are changing from 0 up to 9.6 (in % of the maximum value of the model density).

For the model density five model line projections were calculated for the following equally spaced angles $\varphi = 0.0°$, 11.25°, 22.5°, 33.75°, 45.0°. Next, five functions $\rho_n(p,\Theta)$ were reconstructed employing the CM. Using coefficients from Table I in Ref. 24 it was possible to determine lattice harmonics [thus also radial components $\rho_{l,\nu}(p)$] up to the order $l=30$ and next create new functions $\rho_n(p,\Theta)$. The comparison between densities $\rho(\mathbf{p})$, reconstructed via the CM and NM [with the symmetry requirement (16)], presented in Figs. 2 and 3 shows that the new method improves noticeably the reconstructed densities in the whole momentum range.

V. APPLICATION TO EXPERIMENTAL 2D ACAR SPECTRA IN LaB_6

For the simple cubic compound LaB_6 three 2D ACAR spectra were measured (raw data), for angles $\varphi = 0.0^{\circ}$, 22.5°, 45.0°, and subjected to a deconvolution algorithm (deconvoluted data)—for more details, see Ref. 14. These deconvoluted spectra were used to reproduce three functions $\rho_n(p,\Theta)$ via the CM. Next, radial components $\rho_{l,\nu}(p)$ (up to $l=30$) were determined and new functions $\rho_n(p,\Theta)$ were created up to $n=28$ [neglecting $\rho_{30,\nu}(p)$ that are smaller than the experi-

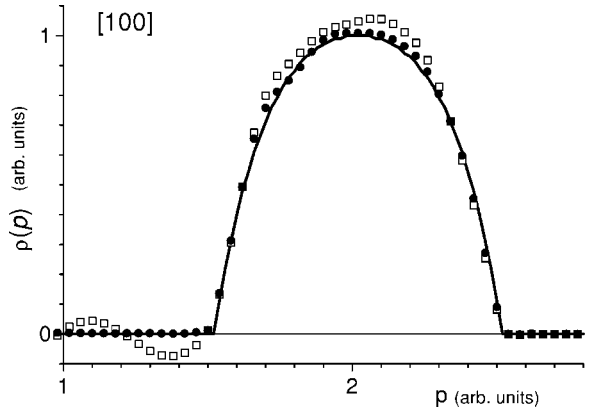

FIG. 3. Densities $\rho(\mathbf{p})$ along the (100) direction reconstructed using the CM (open squares) and NM (solid circles), compared with model (solid line). Their differences were shown in Fig. 2

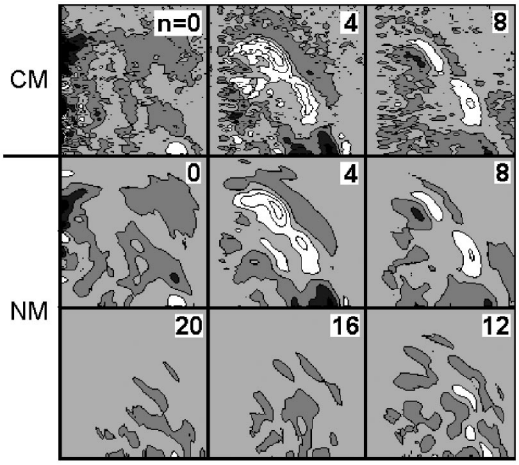

FIG. 4. Functions $\rho_n(p,\Theta)$ for $n\neq 0$ and $\rho_0(p,\Theta)-\rho_{0,1}(p)$, reconstructed employing the CM and NM. Each function is shown in the momentum range 1.38×1.38 (a.u.)^2 (atomic units of momentum)^2, and the lighter colors denote the higher values.

mental noise]. Some of densities $\rho_n(p,\Theta)$ are displayed in Fig. 4. In order to show their details, we subtracted from $\rho_0(p,\Theta)$ the isotropic component $\rho_{0,1}(p)$, being the isotropic average of the 3D density $\rho(\mathbf{p})$ and calculated from $\rho_0(p,\Theta)$ using Eq. (14) for $l=0$.

It is seen that both general shape and magnitude of the three first functions $\rho_n(p,\Theta)$ reconstructed via the CM and NM are very similar, although the NM filters the experimental noise. However, in the case of the NM it was possible to create new functions $\rho_n(p,\Theta)$ with $n\geqslant 12$. It is visible that the series is slowly convergent and at least functions with $n=12$ and 16 should not be neglected in $\rho(\mathbf{p})$. This is proved by results displayed in Figs. 5 and 6 showing the anisotropic part of densities obtained via the CM($m=3$) and NM($m=3$), where m denotes the number of functions $\rho_n(p,\Theta)$ in $\rho(\mathbf{p})$. It

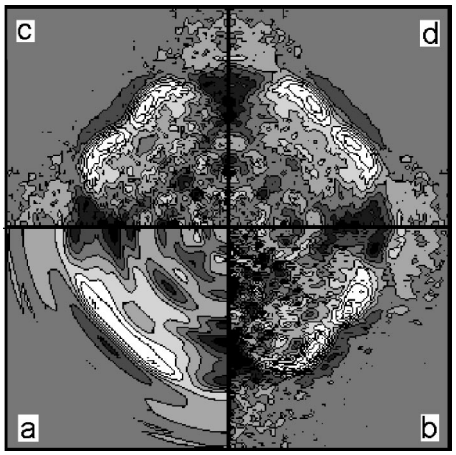

FIG. 5. The anisotropy of densities: $\rho(\mathbf{p})-\rho_{0,1}(p)$ in LaB_6, reconstructed via the CM(3). Parts (a) and (b) show, respectively, reconstructed densities on the (001) and (100) planes. Parts (c) and (d) display, respectively, densities after symmetrization on the (100) plane and in the whole space [after requirement (16)]. The momentum range in each part is 1.6×1.6 (a.u.)^2 and the lighter colors denote the higher values.

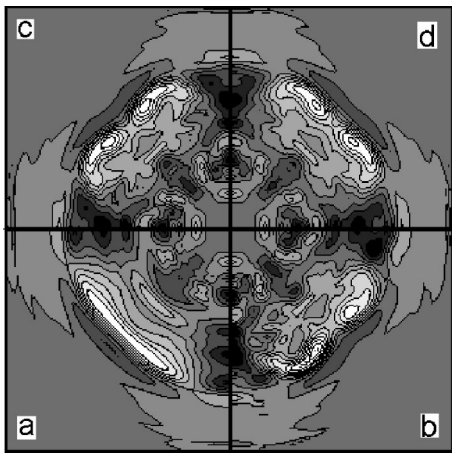

FIG. 6. The same as in Fig. 5 but for the NM(3).

is clear that three first functions $\rho_n(p,\Theta)$ are not sufficient for description of densities because there are large discrepancies between results on planes (001) and (100) both for the CM and NM. Only in the case of using at least five $\rho_n(p,\Theta)$, densities on these two planes are the same, i.e., the symmetry requirement (16) is automatically fulfilled. However, densities reconstructed by the CM(3) and NM with imposing this requirement do not differ too much, although the use of new $\rho_n(p,\Theta)$ filters the experimental noise and introducing new higher $\rho_n(p,\Theta)$ enhances the anisotropy (similarly to deconvolution procedure). This result is clearly visible in Fig. 7 where densities $\rho(\mathbf{k})$ [$\rho(\mathbf{p})$ folded into the first BZ (Ref. 27)] for different reconstruction algorithms and along the main symmetry directions are presented.

According to the method proposed in Ref. 28, the intersection of $\rho(\mathbf{k})$ for CM(3) and NM(8) could be used to determine the experimental Fermi momenta k_F (if the corresponding elements of the FS were big enough). For the XR and XM directions thus estimated k_F are equal to 0.248 and 0.266 atomic units of momentum (a.u.), respectively. Using the maximum gradient procedure proposed in Ref. 26 the following values of k_F were found (a.u.): 0.245, 0.251, 0.245 (along XR) and 0.267, 0.266, 0.266 (along XM) for cases CM(3), NM(3), NM(8), respectively. These values are in

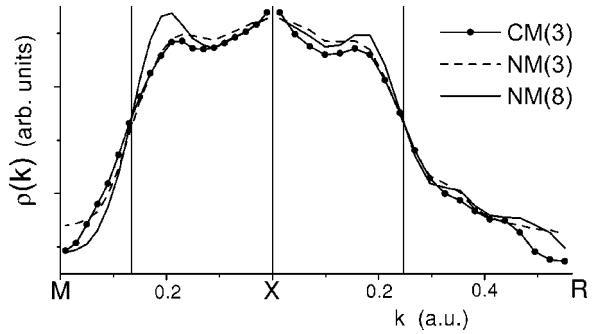

FIG. 7. Densities $\rho(\mathbf{k})$ in LaB_6 along the XR and XM directions, reconstructed by various techniques [CM(3), NM(3), NM(8)] and normalized to the same volume in the whole space $\mathbf{k}$. Two vertical lines on the XR and XM directions show the positions where densities ρ(k) of the CM(3) and NM(8) intersect.

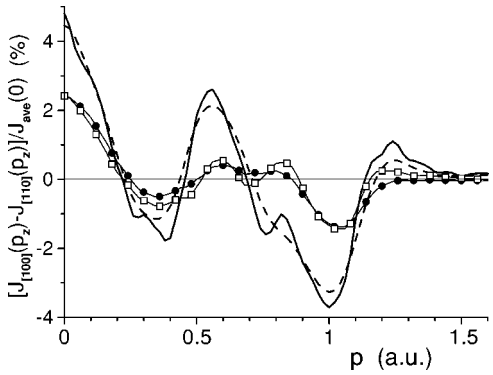

FIG. 8. Differences between ID ACAR spectra in LaB_6 for directions [100] and [110] [in % of the average value of $J(p_z=0)$ for given kind of spectra]. Solid and dashed lines display differences for theoretical and convoluted theoretical spectra, respectively. Lines with circles and squares denote differences for raw and deconvoluted experimental profiles, respectively.

very good agreement with theoretical APW band structure results[8] [$k_F=0.249$ and 0.266 (a.u.) for XR and XM, respectively] but they are somewhat bigger than FLAPW results[16] [equal to 0.243 and 0.256 (a.u.) for the XR and XM directions, respectively]. Along the ΓM direction there are two hole-elements that are too narrow to be reproduced properly within the experimental resolution. However, the comparison of $\rho(\mathbf{k})$ obtained by the CM(3) and NM(8) suggests that this unoccupied region surrounding the Γ point really exists. The more detailed analysis will be given at the end of the next section.

VI. COMPARISON OF EXPERIMENT WITH THEORY IN LaB_6

Two theoretical 2D ACAR spectra in LaB_6 for angles $\varphi=0.0^{\circ}$, 45.0°, consistent with band-structure results presented in Fig. 2 in Ref. 16, were calculated within the independent particle model (IPM), convoluted with the experimental resolution function and normalized to the same volume as the corresponding experimental ones.[14] First, they were used to create 1D ACAR spectra $J(p_z)$ [plane projections of $\rho(\mathbf{p})$] to study many-body effects. Differences between $J(p_z)$ for the main symmetry directions [c100] and [110] are presented in Fig. 8. They show that the anisotropy of the raw experimental profiles is very similar to the corresponding anisotropy of the convoluted theoretical profiles. However, its magnitude is about 1.5–2.0 times smaller.

Since the electron-positron (*e-p*) correlations are not taken into account in the theory, the normalization of theoretical and experimental spectra to the same volume is problematic.[29] Indeed, due to the *e-p* correlations the core contribution (in the experiment) is smaller in comparison with IPM calculations. However, because there are many valence electrons (27) screening the ions, the core contribution is essentially reduced by the positron wave function, taken into account in the present IPM calculations. Thus, the magnitude of the observed anisotropy of the theoretical spectra has to be enhanced. By doing this we get a similar effect as

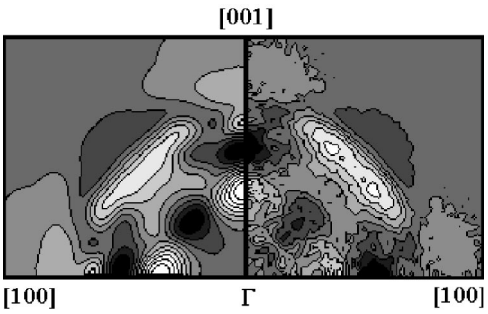

FIG. 9. Densities $\rho(\mathbf{p})-\rho_{0,1}(p)$, reconstructed from two convoluted theoretical (left part) and raw experimental (right part) 2D ACAR spectra (normalized to the same volume). Experimental densities are multiplied by the factor 1.7. The momentum range in each part is 1.6×1.6 (a.u.)^2 and the lighter colors denote the higher values.

observed in the Compton scattering experiments (e.g., Ref. 30, and references therein)—the anisotropy of the theoretical 1D spectra about two times higher than for experimental ones.

The effect of diminishing the anisotropy of experimental profiles may point out the *e-e* correlation effect, suggested in Ref. 16, observed in Compton scattering experiments and studied in detail for both ACAR and Compton 1D data in Y.[31] This effect is interpreted as *e-e* correlations for the following reasons. According to all theoretical investigations (performed for electron gas, see Ref. 32 and references in Ref. 31) *e-e* correlation effects influence the electron momentum density by increased smearing the FS and by the appearance of a momentum tail above the Fermi momentum k_F. As a consequence the anisotropy of profiles becomes lower.

The analogous behavior (indicating strong *e-e* correlations) is observed for functions $N_0(p,\Theta)$ and $N_4(p,\Theta)$, determined from two raw experimental and convoluted theoretical 2D ACAR spectra in LaB_6, and for the corresponding $\rho_0(p,\Theta)$, $\rho_4(p,\Theta)$, and $\rho(\mathbf{p})$, the last displayed in Fig. 9. In order to show its details, we present only its anisotropic part $\rho_0(\mathbf{p})-\rho_{0,1}(p)$. In this figure results for experimental raw data (previously normalized to the theoretical spectra) had to be multiplied by the factor 1.7 to get anisotropy of a similar order as for the convoluted theory.

The observation of *e-e* correlations in the positron annihilation experiment is very important because all theories, apart from the theory presented in Ref. 33, devoted to the many-body effects in the *e-p* annihilation (e.g., Ref. 34, and references therein) are based on the Carbotte and Kahana results.[35] According to them the dynamic parts of the "direct" *e-p* and *e-e* interactions cancel themselves and one should observe only the static part of the *e-p* interaction. Our studies of the many-body effects in yttrium concluded that the static part of the "direct" *e-p* interaction (so-called enhancement) is rather momentum-independent,[36] in agreement with Bloch Modified Ladder (BML) theory results (*e-p* interaction is introduced via lattice[37]). Next, the simultaneous analysis of Compton scattering and positron annihilation experiments allowed to observe strong *e-e* correlations not only in the Compton scattering but also in the positron annihilation experiment.[31]

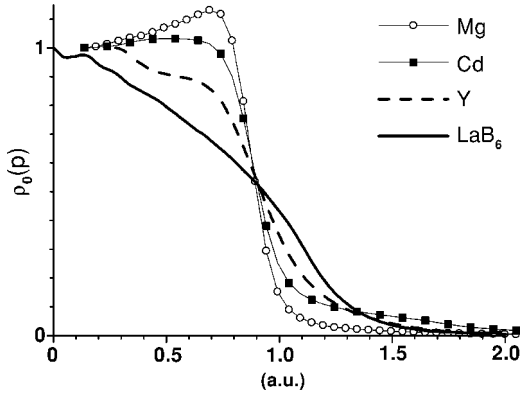

FIG. 10. $\rho_{0,1}(p)$ reconstructed from 2D ACAR data for various metals (for details see text).

In Fig. 10 the isotropic component of densities, $\rho_{0,1}(p)$, reconstructed from three experimental 2D ACAR spectra in LaB_6, is compared with $\rho_{0,1}(p)$ for Y,[31] Mg and Cd.[38]

Densities for Y, Mg, and Cd were shifted to have the value $[\rho_{0,1}(p)/\rho_{0,1}(p=0)]=0.5$ for the same momentum p as in LaB_6. In this way we can compare the momentum densities in these metals close to their averaged FS's, which, however, do not have to occur for $[\rho_{0,1}(p=p_F)/\rho_{0,1}(0)]=0.5$. It shows that only for Mg there is *Kahana-type* enhancement with its typically strong momentum dependence. Such an enhancement is in agreement with different *e-p* interaction theories [e.g., BML and LDA (Ref. 39)]. The same behavior was observed for Cu where a significant hybridization between 4*s* and 3*d* electrons is present and both theories BML and LDA showed a *Kahana-type* enhancement, proved also by the experiment.[40] For yttrium some *e-p* interaction theories (for more details see, Ref. 36) suggested a *Kahana-type* enhancement, too. However, the experiment (Ref. 31, and references therein) detected no enhancement, in agreement with the results of BML, which resembled the results of IPM. Such a lack of a momentum dependence of the *e-p* enhancement in Y is caused by strong lattice effects (intraband and interband transitions). It seems that the same situation (lack of momentum dependent *e-p* enhancement) is observed in LaB_6. Concerning the electronic structure studies, the good agreement between theoretical and corresponding experimental data suggests that the electronic structure of LaB_6 is well described by the FLAPW theory (see Figs. 8 and 9). Thus, because the observed smearing of $\rho_{0,1}(p)$ is much and much stronger than in convoluted theoretical $\rho_{0,1}(p)$ it must follow from strong *e-e* correlations (such a conclusion was also drawn after the previous analyzes).

It is known that it is not possible to get FS from $\rho(\mathbf{p})$ because $\rho(\mathbf{p}=\mathbf{p}_F)$ is not a constant value. However, one can try to obtain some information from the function $\rho(\mathbf{p})-\rho_{0,1}(p)$ (presented in Fig. 11) that corresponds to the anisotropy of densities around the "averaged FS." Namely, the isodensities in Figs. 5, 6, 9, and 11(c) are nearly parallel to the BZ boundaries along the line $\Sigma \equiv \Gamma M$. In the case of densities reconstructed from the theoretical 2D ACAR spectra, they produce a FS where states along ΓM are empty (see black color in Fig. 13(a) shown further). Indeed, the consequent reconstructed FS does not show the ellipsoid necks but

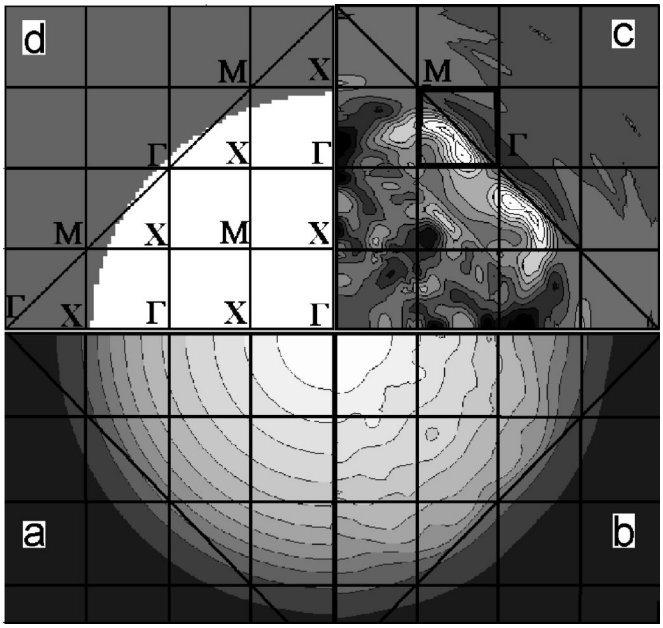

FIG. 11. Densities on the plane (001), reconstructed by NM(8) from three deconvoluted 2D ACAR spectra: $\rho_{0,1}(p)$—part (a), $\rho(\mathbf{p})$—part (b), and $\rho(\mathbf{p})-\rho_{0,1}(p)$—part (c), compared with the free-electron sphere containing 27 electrons—part (d). All parts are drawn with some BZ boundaries.

is very close to the Σ line. However, calculations of theoretical densities $\rho(\mathbf{p})$ (from which 2D ACAR spectra were created) were performed for a limited mesh (35 points) inside the irreducible part of the BZ. Thus, densities reconstructed from the theoretical spectra are probably missing the details required to reproduce the necks appropriately. Nevertheless, we note that a good deal of the anisotropic part of the *e-p* momentum density in the $\mathbf{p}$ space reflects the general features of the FS [a similar procedure has been already applied in Ref. 41 for line projections of $\rho(\mathbf{p})$ in CeB_6]. This observation is a basis to the interpretation of our experimental results, presented detailed in Fig. 12.

The experimental densities indicate that the FS crosses the ΓM line [Figs. 12(a) and 12(c)]. For sake of comparison, we drew the same anisotropic part of the densities reconstructed by the CM(3) [Fig. 12(e)]. In this case the above feature is not seen—this is observed only for the NM(8) and *drawn* by components $\rho_n(p,\Theta)$ for $n \geqslant 8$ [Fig. 12(d)]. As it was shown by different tests and is seen in Fig. 7 here the NM works as a deconvolution procedure (i.e., enhances anisotropy) and thus allows us to detect some subtle details. So, the observed fine feature is connected with neither the effect of bigger smearing of the experiment by *e-e* correlations nor the experimental error [density components in Fig. 12(d) do not have an oscillating character and the prominent element is visible].

Due to the above considerations, it seems that we observe small electron pockets in the next (15th) band around the Σ line, detected by some dHvA experiments.[8,10] It is worth noticing that the group symmetry character of the 15th band along the $\Gamma M(\Sigma)$ line is Σ_4 (see Refs. 8 and 16). As such, its contribution to the momentum density in the

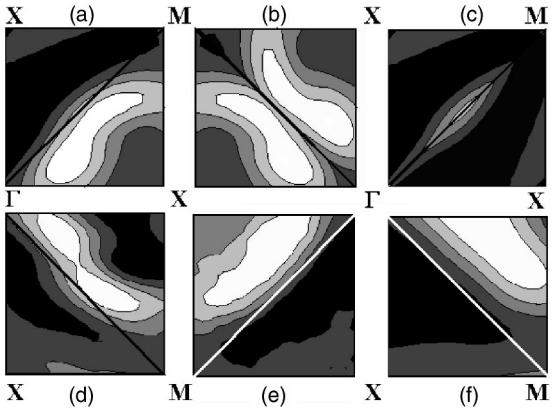

FIG. 12. $\rho(\mathbf{p})-\rho_{0,1}(p)$ reconstructed from three deconvoluted experimental 2D ACAR spectra via NM(8) and CM(3) [quadrants (a) and (e), respectively] and from two convoluted theoretical spectra [quadrant (f)], in the same part of **p** space as marked by thickened square in Fig. 11(c). Quadrants (b) and (c) show elements of quadrant (a) from the 14th and 15th bands, respectively, mirrored about the Γ*M* diagonal. Densities from quadrant (a) after subtracting $\rho_4(p,\Theta)$ are displayed in (d).

first BZ and higher BZ's, where **p** is parallel to **k**, vanishes, as discussed by Harthorn *et al.* (see Ref. 42). However, it may appear for $\mathbf{p}=\hbar(\mathbf{k}+\mathbf{G})$ with reciprocal lattice vectors $\mathbf{G}=(2\pi/a)(\xi,\eta,0)$, where $\xi\neq\eta\neq 0$. Thus, it can contribute along such ΓM lines that are parallel to the XX line from the first BZ [see Fig. 11(c)]. In the extended zone **p** the 14th (Σ_1) and 15th (Σ_4) bands occur in the part of the **p** space marked by the thickened square in Fig. 11(c). In this area, there are the biggest contribution to the total densities $\rho(\mathbf{p})$ coming from the 14th band (below the ΓM line) and from the 15th band (above this line). Thus, some details of the FS just in this region were able to be observed.

In the case of the theoretical calculations these elements may only be obtained if the spin-orbit interaction is included in the band structure calculations as well as the $4f$ level is displaced upward by 0.1 Ry (which may correspond to self-interactions and/or the nonlocal corrections to LDA—for more details, see Refs. 8 and 16) and do not appear in Fig. 12(f).

Finally, by looking at the densities $\rho(\mathbf{k})$ obtained by applying the LCW transformation to $\rho(\mathbf{p})$ and presented in the part 3 of Fig. 13, it appears that $\rho(\mathbf{k})$ derived from two convoluted theoretical spectra are not able to reproduce the unoccupied region surrounding the Γ point (the corresponding dHvA frequency is denoted as ϵ in Refs. 2 and 9. This inability is due to resolution smearing (compare with part 2 of Fig. 13) as well as the positron wave function effect, demonstrated in Fig. 12(a) of Ref. 16. Namely, *e-p* **k**-space density $\rho(\mathbf{k})$ (calculated within IPM for the 13 fully occupied valence bands) at the Γ point is significantly higher than at M. This effect is due to a different orbital character of the electron states. Moreover, *e-p* correlations should enhance this effect—the more localized electron, the lower probability of its annihilating. The smaller size of the unoccupied region around Γ (having linear dimensions of the order of the experimental resolution) compared to the unoccupied region

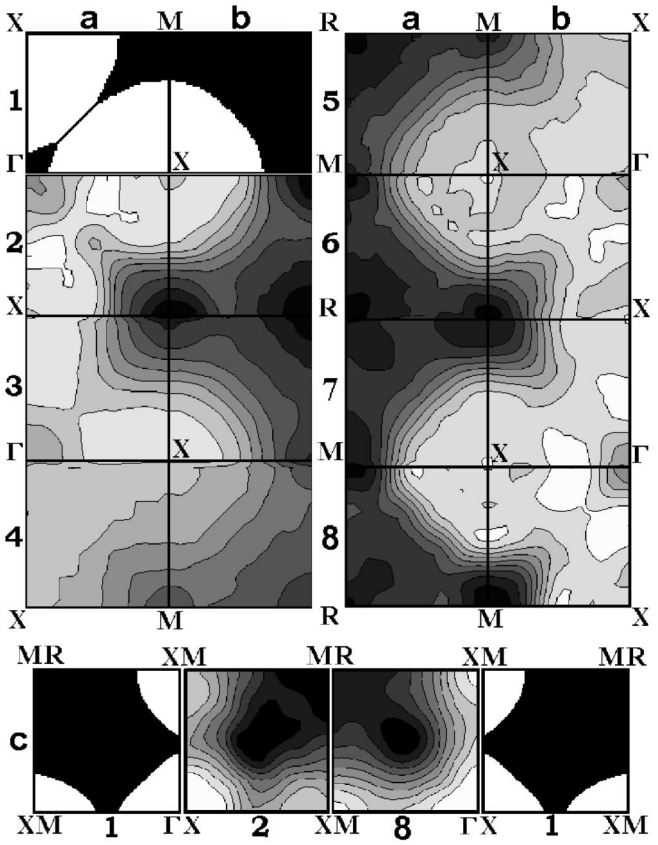

FIG. 13. Densities $\rho(\mathbf{k})$ in LaB_6 compared with the theoretical occupancy in the 14th band (Ref. 16) (part 1, where white areas denote occupied states). Densities reconstructed from two 2D ACAR spectra are presented in parts 2 to 4 for: 2—theory, 3—theory convoluted with the experimental resolution, 4—raw experimental data. Next parts display densities reconstructed from three raw (part 5) and three deconvoluted (parts 6–8) experimental data for cases: CM(3) (parts 5–6), NM(3) (part 7), NM(8) (part 8). Panels (a), (b), and (c) show densities on parallel planes distant from the Γ point at 0, π/a, and $\pi/2a$, respectively, where a is the lattice constant.

around M increases the effect. However, after applying the new filtering procedure (parts 7 and 8), which not only filters the experimental noise but also enhances the anisotropy of the densities, $\rho(\mathbf{k})$ around the Γ is decreased. Thus, we can confirm the existence of the region ϵ, detected also in dHvA experiments.[1–3,6] Indeed, ϵ is also observed in the **p** space [Fig. 12(b)] and the FS is in good agreement with the theory. Similarly to what observed in **p** space (recall Fig. 9), the anisotropy of $\rho(\mathbf{k})$ is diminished, which proves again the *e-e* correlation effect.

VII. SUMMARY

The proposed technique of filtering reconstructed densities was applied to the cubic model and to 2D ACAR spectra in LaB_6. The method not only filters the experimental noise but slightly enhances some details of the reconstructed densities as well.

Experimental 2D ACAR spectra for LaB_6 were interpreted in terms of both 1D projections (to study *e-e* correlation effects) and reconstructed 3D densities both in the extended **p** and reduced **k** spaces. Due to the simultaneous (using the same procedures) analysis of theoretical (for merely two main symmetry directions) and experimental 2D ACAR spectra and the corresponding densities as well, the following conclusions can be drawn for LaB_6:

(1) The IPM describes the experimental data well and the typical momentum-dependent *e-p* enhancement is not observed. This effect is somewhat surprising because according to the electronic structure calculations,[8,16] bands crossing the Fermi level are parabolic. Thus, one could expect some momentum-dependence of the *e-p* enhancement.

(2) The small magnitude of the anisotropy of the experimental densities points out strong anisotropic *e-e* correlations, in agreement with the suggestion in Ref. 16. This is a very important result because almost all theoretical approaches devoted to the many-body effects in the *e-p* annihilation are based on the Carbotte and Kahana results[35] and hint that the momentum-dependent *e-e* correlations should not be observed in the *e-p* annihilation experiment.

(3) Electron states (both topology of FS and character of bands, seen in the positron annihilation experiment) in LaB_6 are well described by the FLAPW band theory. However, detailed analysis of densities in **p** space (we excluded smearing effects, experimental noise, etc.) showed that the anisotropic part of the densities clearly reflects the fact that there are necks in the the 14th band. Moreover, from our analysis in **p** space we conjecture the existence of small additional FS electron pockets in the 15th band observed also in dHvA experiments.[8,10] These pockets, whose sizes are smaller than the limit set by the resolution of the current 2D-ACAR spectrometers, are not detected in **k** space (there is no such possibility to reproduce remarkably high jump of densities $\rho(\mathbf{k})$ in this small region). However, the comparative analysis in **p** space between the theoretical data utilized here (where no such FS sheet occurs) and the experimental data, reconstructed adopting the NM presented in this paper, shows additional density consistent with our conjecture.

Therefore, this special filter seems to be a promising tool to reveal fine features of the *e-p* momentum density until now precluded to the 2D ACAR experiments.

ACKNOWLEDGMENTS

We are very grateful to the Polish State Committee for Scientific Research (Grant No. 2 P03B 012 25) for the financial support.

[1] A.J. Arko, G. Crabtree, D. Karim, F.M. Mueller, L.R. Windmiller, J.B. Ketterson, and Z. Fisk, Phys. Rev. B **13**, 5240 (1976).

[2] Y. Ishizawa, T. Tanaka, E. Bannai, and S. Kawai, J. Phys. Soc. Jpn. **42**, 112 (1977).

[3] Y. Ishizawa, H. Nozaki, T. Tanaka, and T. Nakajima, J. Phys. Soc. Jpn. **48**, 1439 (1980).

[4] M. Aono, T.-C. Chiang, J.A. Knapp, T. Tanaka, and D.E. Eastman, Phys. Rev. B **21**, 2661 (1980).

[5] Y. Onuki, N. Nishihara, M. Sato, and T. Komatsubara, J. Magn. Magn. Mater. **52**, 317 (1985).

[6] T. Suzuki, T. Goto, S. Sakatsume, A. Tamaki, S. Kunii, T. Kasuya, and T. Fujimura, Jpn. J. Appl. Phys., Suppl. **26-3**, 511 (1987).

[7] W. Joss, J.M. van Ruitenbeek, G.W. Crabtree, J.L. Tholence, A.P.J. van Deursen, and Z. Fisk, Phys. Rev. Lett. **59**, 1609 (1987).

[8] H. Harima, O. Sakai, T. Kasuya, and A. Yanase, Solid State Commun. **66**, 603 (1988).

[9] Y. Onuki, T. Komatsubara, P.H.P. Reinders, and M. Springford, J. Phys. Soc. Jpn. **58**, 3698 (1989).

[10] H. Matsui, T. Goto, S. Kunii, and S. Sakatsume, Physica B **186–188**, 126 (1993).

[11] N. Harrison, P. Meeson, P.-A. Probst, and M. Springford, J. Phys.: Condens. Matter **5**, 7435 (1993).

[12] S. Tanigawa, T. Kurihara, M. Osawa, T. Komatsubara, and Y. Onuki, in *Positron Annihilation*, edited by L. Dorikens-Vanpraet, M. Dorikens, D. Segers (World Scientific, Singapore, 1989), p. 239.

[13] M. Biasini, H.M. Fretwell, S.B. Dugdale, M.A. Alam, Y. Kubo, H. Harima, and N. Sato, Phys. Rev. B **56**, 10 192 (1997).

[14] M. Biasini, M.A. Monge, G. Kontrym-Sznajd, M. Gemmi, and N. Sato, Mater. Sci. Forum **363–365**, 582 (2001).

[15] A. Hasegawa and A. Yanase, J. Phys. F: Met. Phys. **7**, 1245 (1977); A. Yanase and A. Hasegawa, in *Electron Correlation and Magnetism in Narrow-Band Systems*, edited by T. Moriya (Springer-Verlag, Berlin, 1981), p. 230, and references therein.

[16] Y. Kubo, S. Asano, Phys. Rev. B **39**, 8822 (1989). In this paper theoretical results in terms of $\rho(\mathbf{k})$ were compared with the corresponding experimental results in Ref. 12.

[17] Gabor T. Herman, *Image Reconstruction from Projections* (Academic, New York, 1980).

[18] S.R. Deans, *The Radon Transform and Some of Its Applications* (Wiley, New York, 1983).

[19] F. Natterer, *The Mathematics of Computerized Tomography* (Wiley, Stuttgard, 1986).

[20] S. Berko, in *Proc. Int. School Phys. Enrico Fermi Course LXXXIII*, edited by W. Brandt and A. Dupasquier (North-Holland, Amsterdam, 1983), p. 64.

[21] A.M. Cormack, J. Appl. Phys. **34**, 2722 (1963); **35**, 2908 (1964).

[22] G. Kontrym-Sznajd, Phys. Status Solidi A **117**, 227 (1990).

[23] All algorithms where the reconstruction of 3D density is reduced to a set of reconstruction of 2D densities, performed independently on some planes p_y'=const., e.g. R.A. Brooks and G. Di Chiro, Phys. Med. Biol. **21**, 689 (1976) (filtered back projection technique); R. Suzuki, M. Osawa, S. Tanigawa, M. Matsumoto, and N. Shiotani, J. Phys. Soc. Jpn. **58**, 3251 (1989) (Fast Fourier Transform) or CM, described in Chap. II.

[24] F.M. Mueller and M.G. Priestley, Phys. Rev. **148**, 638 (1966).

[25] *Handbook of Mathematical Functions*, edited by M. Abramowitz and J.A. Segun (Dover, New York, 1968).

[26] M. Biasini, G. Ferro, G. Kontrym-Sznajd, and A. Czopnik, Phys. Rev. B **66**, 075126 (2002).
[27] D.G. Lock, V.H.C. Crisp, and R.N. West, J. Phys. F: Met. Phys. **3**, 561 (1972).
[28] S.B. Dugdale, H.M. Fretwell, M.A. Alam, G. Kontrym-Sznajd, R.N. West, and S. Badrzadeh, Phys. Rev. Lett. **79**, 941 (1997).
[29] In the case of the ACAR data we do not measure the absolute value of the momentum density $\rho(\mathbf{p})$. Due to the presence of the positron, the normalization of the spectra is somewhat ambiguous, in contrary to the Compton spectra, where the field of the Compton profile is equal to the number of valence electrons.
[30] S. Huotari, K. Hämäläinen, S. Manninen, S. Kaprzyk, A. Bansil, W. Caliebe, T. Buslaps, V. Honkimäki, and P. Suortti, Phys. Rev. B **62**, 7956 (2000).
[31] G. Kontrym-Sznajd, M. Samsel-Czekala, A. Pietraszko, H. Sormann, S. Manninen, S. Huotari, K. Hämäläinen, J. Laukkanen, R.N. West, and W. Schülke, Phys. Rev. B **66**, 155110 (2002).
[32] L. Lam and P.M. Platzman, Phys. Rev. B **9**, 5122 (1974).
[33] J. Arponen and E. Pajanne, Ann. Phys. (N.Y.) **121**, 343 (1979).
[34] M. Šob, H. Sormann, and J. Kuriplach, Adv. Quantum Chem. **42**, 77 (2003); A. Rubaszek, Z. Szotek, and W.M. Temmerman, Phys. Rev. B **65**, 125104 (2002).
[35] J.P. Carbotte, and S. Kahana, Phys. Rev. **139**, A213 (1965).
[36] H. Sormann, G. Kontrym-Sznajd, and R.N. West, Mater. Sci. Forum **363–365**, 609 (2001); H. Sormann (unpublished).
[37] H. Sormann, Phys. Rev. B **54**, 4558 (1996).
[38] A. Jura, G. Kontrym-Sznajd, and M. Samsel-Czekala, J. Phys. Chem. Solids **62**, 2241 (2001).
[39] S. Daniuk, G. Kontrym-Sznajd, A. Rubaszek, H. Stachowiak, J. Mayers, P.A. Walters, and R.N. West, J. Phys. F: Met. Phys. **17**, 1365 (1987).
[40] F. Sinclair, W.S. Farmer, and S. Berko, in *Positron Annihilation*, edited by P.G. Coleman, S.C. Sharma, and L.M. Diana (North-Holland, Amsterdam, 1982), p. 322.
[41] M. Biasini, M.A. Alam, H. Harima, Y. Onuki, H.M. Fretwell, and R.N. West, J. Phys.: Condens. Matter **6**, 7823 (1994).
[42] R. Harthoorn and P.E. Mijnarends, J. Phys. F: Met. Phys. **8**, 1147 (1978).